

## ULTRAFAST DYNAMICS

# Attosecond dynamical Franz-Keldysh effect in polycrystalline diamond

M. Lucchini,<sup>1\*</sup> S. A. Sato,<sup>2</sup> A. Ludwig,<sup>1</sup> J. Herrmann,<sup>1</sup> M. Volkov,<sup>1</sup> L. Kasmi,<sup>1</sup> Y. Shinohara,<sup>3</sup> K. Yabana,<sup>2</sup> L. Gallmann,<sup>1,4</sup> U. Keller<sup>1</sup>

Short, intense laser pulses can be used to access the transition regime between classical and quantum optical responses in dielectrics. In this regime, the relative roles of inter- and intraband light-driven electronic transitions remain uncertain. We applied attosecond transient absorption spectroscopy to investigate the interaction between polycrystalline diamond and a few-femtosecond infrared pulse with intensity below the critical intensity of optical breakdown. Ab initio time-dependent density functional theory calculations, in tandem with a two-band parabolic model, accounted for the experimental results in the framework of the dynamical Franz-Keldysh effect and identified infrared induction of intraband currents as the main physical mechanism responsible for the observations.

During the 1980s, rapid progress in picosecond and femtosecond ultrafast lasers started to bridge the gap between electronics and optics (1). The resulting synergy has since given rise to a wealth of new technologies and scientific insights, such as the optical generation of terahertz frequencies for the investigation of ever faster physical processes and device performance (2, 3). The more recent progress in ultrafast laser sources, which now produce few-cycle femtosecond (4) and attosecond (5, 6) pulses with full electric field control (7), extends these ideas into the petahertz frequency regime. Indeed, using measurement concepts similar to those developed for terahertz electric fields and femtosecond time resolution, we now can explore the speed limits of electronics at optical frequencies with methods such as attosecond transient absorption spectroscopy (ATAS) (8–10), which has recently been extended to solid-state materials (11–13). This has opened the possibilities of studying electron motion under the influence of a high-frequency electric field and of investigating the feasibility of petahertz electronic devices (14, 15).

Here, we used ATAS to explore a regime where the electrons in a dielectric material are exposed to a relatively strong high-frequency optical field. In this case, the quiver energy (or ponderomotive energy  $U_p$ ) of the electrons in the oscillating electrical field becomes comparable to the photon energy of the driving laser. The system transitions from a more quantum-mechanical (photon-driven) to a more classical (field-driven) regime (16). Although both limiting regimes have been extensively studied, the many phenomena occurring in the intermediate regime are still not well understood. In this intermediate regime, the material is described by coupled light-matter states, and effects such as band dressing (17), the dynamical Franz-Keldysh effect (18), and Wannier-Stark localization

(19) coexist. Therefore, the total material response exhibits a complex behavior that often cannot be easily framed within only one of these effects. As a consequence, in this regime the role of intra- and interband transitions in determining the dynamical response of dielectrics also remains unclear (20, 21).

A fundamental process related to the intraband motion of charges is the Franz-Keldysh effect. In a simple physical picture, a static external field applied to a dielectric bends the crystal potential and accelerates the electron-hole pair. Its wave function becomes an Airy function with an exponential tail that extends into the energy gap. As a result, photon-assisted tunneling through a distance that depends on the field strength can happen also for photon energies below the gap (22). When the static field is replaced by a time-dependent one, the response of the system is described by the dynamical Franz-Keldysh effect (DFKE) (23). In addition to the absorption within the band gap, one observes also an induced transparency above the band gap and the appearance of optical side bands (18). In contrast to resonant processes, the DFKE is an ultrafast nonresonant process in which no real carriers are created. It is therefore expected to be fast (24). To date, the DFKE has been observed only around the energy gap of dielectrics (25) and in the terahertz regime (i.e., picosecond time scales) where recent time-resolved studies have shown a nontrivial phase evolution (23). The observation of the DFKE at higher frequencies (i.e., femtosecond time scales) requires higher pump field strengths. At these field intensities, other effects such as multiphoton ionization will dominate the optical response of dielectrics around the band gap. The DFKE is expected to remain observable, but deeper in the conduction band (CB) at higher probing energies.

We used attosecond pulses with duration of ~250 as, centered at ~42 eV, to study field effects such as the DFKE in the high-energy part of the CB of polycrystalline diamond when exposed to a few-femtosecond intense infrared (IR) laser field (IR intensity in vacuum  $I_{\text{IR}} \approx 1 \times 10^{12}$  W/cm<sup>2</sup>). The transient absorption coefficient exhibits sub-femtosecond dynamics with a complex energy-

dependent phase relation. Ab initio calculations performed by coupling time-dependent density functional theory (TDDFT) in real time with Maxwell's equations reproduce the experimental results. We used an orbital decomposition approach to disentangle the complexity of the numerical model and address independently the contribution of each electronic subband. With this approach, we can demonstrate that predominantly one valence band (VB) to CB transition determines the qualitative behavior of the optical response of diamond in the energy range under examination.

Figure 1A shows a schematic of the experimental setup (26, 27). Extreme ultraviolet (XUV) single attosecond pulses and 5-fs phase-locked IR pulses (center energy  $\hbar\omega_0 \approx 1.58$  eV) are focused on a double target composed of a gas jet and a solid sample. Both pulses are linearly polarized along the same axis. The few-cycle IR pulse acts as a pump, inducing dynamics that are then probed by the XUV pulse. The temporal properties of the pump and probe pulses are recorded simultaneously with the diamond transient absorption scan by acquiring a streaking trace from Ne atoms in a scheme similar to the one reported in (17) (Fig. 1B). In this way it is possible to unambiguously calibrate the pump-probe delay axis with respect to the pump electric field. The spectrum of the single attosecond pulses (SAPs) (Fig. 1C, black) spans from 30 to 55 eV and overlaps with the static absorbance for a 50-nm-thick polycrystalline diamond sample (Fig. 1C, blue). The smooth behavior of the absorbance reflects the absence of sharp resonant transitions in this spectral range. The XUV pulse can only excite electrons from the VB to the high part of the CB by single-photon absorption (Fig. 1, D and E). At our experimental intensities, the IR field is also expected to inject electrons into the CB by multiphoton ionization as suggested by a Keldysh parameter,  $\gamma_K \approx 3$  (27, 28). However, the IR pulse can efficiently inject electrons only from the top of the VB to the bottom of the CB. Therefore, even if the IR pulse populates the CB almost 1000 times as efficiently as the attosecond pulse, the contribution coming from direct charge injection by the IR pump pulse in the spectral region of the CB probed by the XUV pulse is negligible.

We investigated the dynamical optical response of the VB and CB of diamond by looking at the IR-induced absorbance,  $\Delta\text{Abs}(E_{\text{ph}}, \tau)$ , defined as the logarithm of the ratio of the transmitted XUV spectral intensities without and with the IR pump (27). Here,  $E_{\text{ph}}$  represents the XUV photon energy and  $\tau$  the pump-probe delay. The experimental results for an IR intensity (in vacuum) of  $\sim 6.5 \times 10^{12}$  W/cm<sup>2</sup> are shown in Fig. 2A. For small values of the delay  $\tau$ , we observe the appearance of transient features that oscillate with  $2\omega_0$  over almost all the bandwidth of the SAP. The main feature lies at an excitation energy of ~43 eV and corresponds to an absorption increment. Figure 2C shows the IR electric field  $E_{\text{IR}}(t)$  extracted from a simultaneous streaking measurement together with the IR-induced absorbance averaged over three energy bands 2 eV wide and centered at 39, 43, and 48 eV. As can be observed, both the

<sup>1</sup>Department of Physics, ETH Zürich, 8093 Zürich, Switzerland.

<sup>2</sup>Center for Computational Sciences, University of Tsukuba, 305-8577 Tsukuba, Japan. <sup>3</sup>Photon Science Center, University of Tokyo, 113-8656 Tokyo, Japan. <sup>4</sup>Institute of Applied Physics, University of Bern, 3012 Bern, Switzerland.

\*Corresponding author. Email: mlucchini@phys.ethz.ch

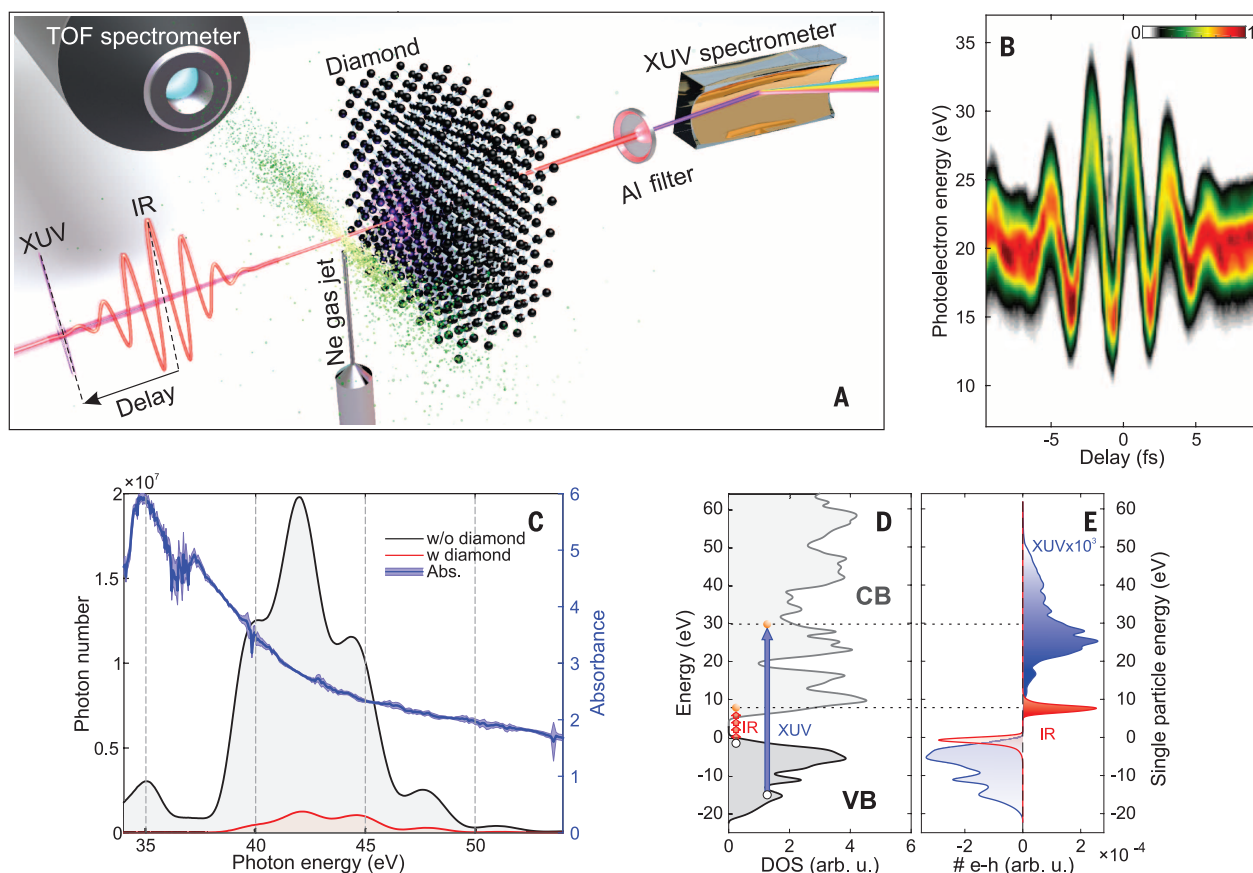


**Fig. 1. Pulse and sample characterization.** (A) Schematic of the experimental setup with the double-target for simultaneous detection of photons and electrons. (B) Example of a typical streaking trace used to characterize the single attosecond pulses (SAPs) and calibrate the pump-probe delay axis in a transient absorption measurement. (C) Spectrum of the SAP without (black line) and with (red line) transmission through a 50-nm polycrystalline diamond sample. The static absorbance measured with a broad harmonic spectrum (27)

is shown in blue. The shaded light-blue area defines the statistical error bars assuming a Poisson distribution for the number of collected photons. (D) Density of states (DOS) of diamond calculated with density functional theory. The black and gray curves are the valence band (VB) and conduction band (CB), respectively. The zero of the energy axis coincides with top of the VB. (E) Number of electron-hole particles created by the XUV probe and the IR pump in blue and red, respectively.

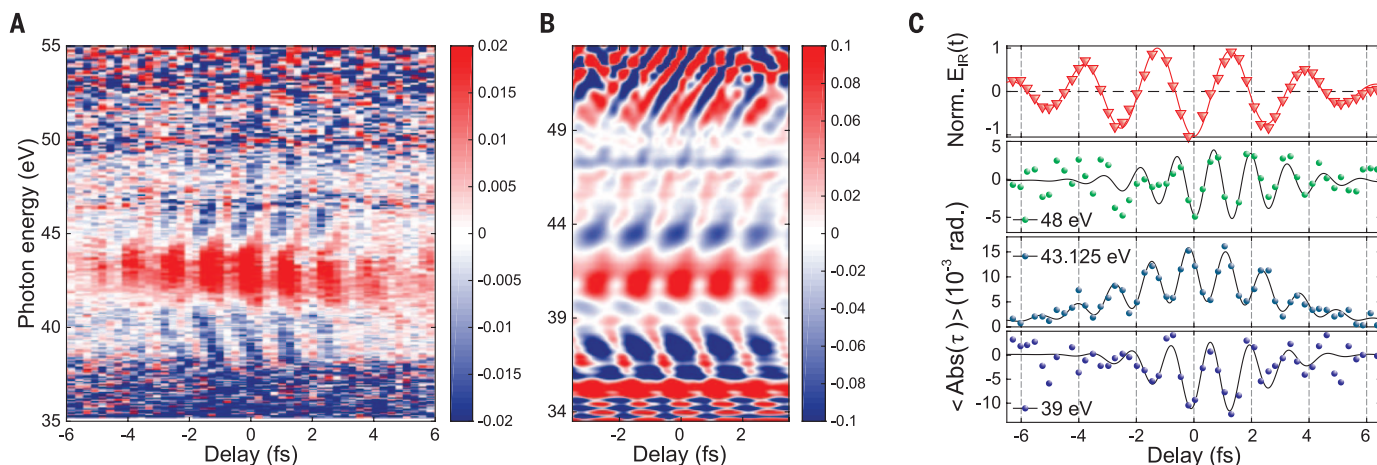


**Fig. 2. Results obtained with single attosecond pulses.** (A and B) Experimental (A) and calculated (B) IR-induced absorbance  $\Delta\text{Abs}(E_{\text{ph}}, \tau)$ . (C) Upper panel: IR electric field  $E_{\text{IR}}(t)$  extracted from a streaking measurement acquired simultaneously with the trace in (A). Lower panels, from bottom to top: Average  $\Delta\text{Abs}$  for three energy bands with a width of  $\sim 2$  eV and centered at 39, 43.1, and 48 eV. In all panels, the markers represent the experimental data. The continuous lines are obtained by fitting the data with an oscillating function  $f(\tau)$  (27). Calculation parameters: IR intensity in vacuum  $I_{\text{IR}} = 5 \times 10^{12}$  W/cm<sup>2</sup>, IR center energy  $\hbar\omega_0 = 1.55$  eV, diamond thickness  $L = 50$  nm.

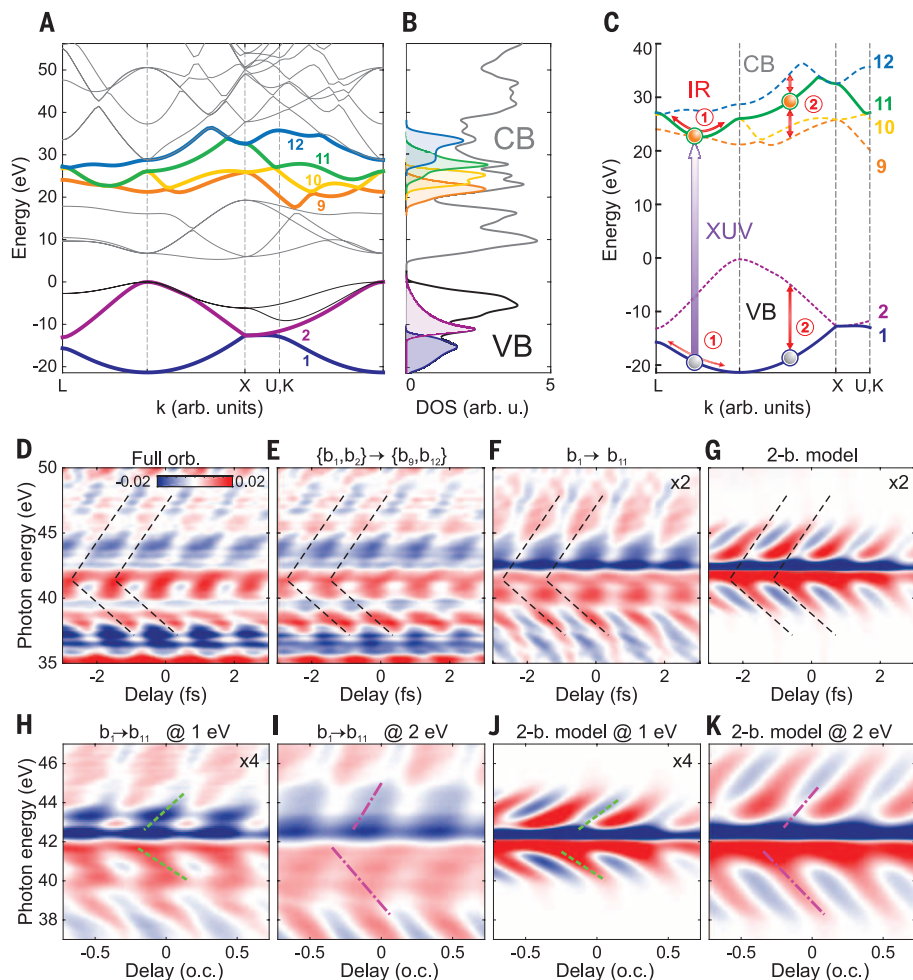


**Fig. 3. Simulation results.** (A and B) Diamond band structure and DOS, respectively. The main subbands dominating the diamond optical response are labeled with numbers and highlighted by a thicker colored line in (A); the same color code is used to mark the DOS of each subband in (B). (C) Cartoon of the two main physical mechanisms induced by the IR pump: (1) intraband motion, (2) interband coupling. (D to G) The 2D color plots show the calculated IR-induced changes in the imaginary part of the dielectric function  $\epsilon(\omega)$ . The first row reports the results for the case of (D) full orbital expansion over the chosen 24 Houston states, (E) transitions between the bands highlighted in (A), (F) transition from  $b_1$  to  $b_{11}$ , and (G) the two-band model. In all panels, the IR intensity inside the diamond is fixed to  $3 \times 10^{12}$  W/cm<sup>2</sup> (27). (H and I) The same results as (F), keeping the same adiabaticity parameter  $\gamma_a$  (32), but for a different IR center energy  $\hbar\omega_0 = 1$  and 2 eV, respectively. (J and K) Same as (H) and (I) but obtained with the two-band model of (G).

position of the maximum of the interaction and the phase of the oscillations increase with increasing energy distance from the main feature at 43 eV. Therefore, the energy dispersion of the oscillating features assumes a V-shape with vertex at 43 eV, which does not follow the pump field adiabatically. The phase delay, extracted from eight independent measurements, between the square of the IR electric field  $E_{\text{IR}}^2(t)$  and the main feature at 43 eV was found to be  $-235 \pm 53$  as.

We simulated the pump-probe experiment using TDDFT in real time (29, 30). The results obtained for a single-crystal cell show that the IR pulse can indeed induce  $2\omega_0$  oscillations in the imaginary part of the transient dielectric function  $\epsilon(\omega)$  and consequently in the absorbance of the material (27). Moreover, whereas the amplitude of the oscillations depends on the crystal orientation with

respect to the light polarization axis, the phase does not change (fig. S8). This phenomenon explains why it is possible to experimentally observe the transient features in a polycrystalline sample. By coupling TDDFT with Maxwell's equations, it is possible to investigate the optical response of the target (27). The numerical results (Fig. 2B) show very good agreement with the experimental results. Both the oscillatory features and the V-shaped energy dispersion are reproduced. All the features in the calculations appear shifted down by almost 1.75 eV in photon energy (the main absorption feature lying at  $\sim 41$  eV instead of 43 eV) because TDDFT fails to reproduce the energy gaps between the subbands in the CB with high accuracy.

To gain further insight into the physical mechanisms involved, we performed an orbital decomposition of the probe Hamiltonian into 24 Houston

states (31), which, when the external IR field vanishes, correspond to the Bloch states depicted in the energy/momentum space of Fig. 3A (27). Figure 3, D and E, shows the pump-induced change in the dielectric function,  $\Delta\epsilon(\omega, \tau)$ , under the same conditions as Fig. 2B except for a single unit cell of diamond (27). The main positive oscillating feature at  $\sim 41$  eV and the V-shaped energy dispersion of the oscillations are still reproduced even when a smaller set of dressed subbands is taken into account, such as two subbands in the VB ( $b_1, b_2$ ) and four in the CB (from  $b_9$  to  $b_{12}$ ). This result is in agreement with the decomposition of the static dielectric function  $\epsilon(\omega)$  (fig. S9). Furthermore, the main qualitative behavior of  $\Delta\epsilon(\omega, \tau)$  can be reproduced by the single transition between the bottom of the VB,  $b_1$ , and the seventh band in the CB,  $b_{11}$  (Fig. 3F). Given the definition of the Houston states used in the decomposition, this result suggests that IR-induced intraband motion, rather than interband transitions (Fig. 3C), is the main physical mechanism dominating the diamond response. To further validate our finding, we calculated  $\Delta\epsilon(\omega, \tau)$  using a parabolic two-band model employed in the DFKE (32). It is derived by parabolic fitting of the energy distance between  $b_1$  and  $b_{11}$  in the crystallographic direction WL. The results (Fig. 3G) reproduce the main qualitative behavior of the TDDFT calculations in Fig. 3F. The main differences between the two models may come from the fact that the two-band model takes into account neither the anisotropy of diamond nor the anharmonic dispersion of its actual electronic bands. The complex dispersion of bands  $b_1$  and  $b_{11}$  indeed suggests that more than a single parabolic fit might be needed to better describe the case of polycrystalline diamond with random orientation (fig. S12).

Finally, we investigated the dependence of  $\Delta\epsilon(\omega, \tau)$  on the IR frequency. The results are plotted in Fig. 3, H to K, for  $\hbar\omega_0 = 1$  and 2 eV. The TDDFT calculations show a clear dependence of the tilt of the oscillating structures as a function of  $\omega_0$  (compare green dashed and violet dash-dotted lines in Fig. 3, H and I). This behavior is well reproduced by the two-band model, thus confirming the dominant role of the DFKE or, in other words, intraband transitions.

Our results demonstrate that attosecond transient absorption spectroscopy can be used to directly investigate the ultrafast electron dynamics in the valence and conduction bands of dielectrics in the intermediate regime of strong optical fields. For the particular case of diamond, the observed dynamics unfold on an attosecond time scale and fully recover after the interaction. A comparison with *ab initio* calculations and a parabolic two-band model allowed us to demonstrate the dominant role of intra- over intersubband transitions, thus moving another step toward a full understanding of optical manipulation of carriers in dielectrics in the petahertz regime. The field strength necessary to observe DFKE in the femtosecond regime is sufficient to inject a substantial number of electrons into the bottom of the CB via multiphoton excitation. Therefore, direct probing of the DFKE

around at the bottom of the CB with mid-IR or terahertz driving fields is impossible (23, 24). Our results, however, prove that it is possible to observe the DFKE driven by femtosecond IR pulses at energies high above the band gap. We have also shown that the fine structure in the transient response of diamond deviates from the simplified parabolic model and thus encodes information about the particular band dispersion of the target.

#### REFERENCES AND NOTES

- D. H. Auston, K. P. Cheung, J. A. Valdmanis, P. R. Smith, *Picosecond Electronics and Optoelectronics* (Springer-Verlag, 1985).
- D. H. Auston, *Top. Appl. Phys.* **60**, 183 (1988).
- D. Grischkowsky, S. Keiding, M. van Exter, C. Fattinger, *J. Opt. Soc. Am. B* **7**, 2006 (1990).
- G. Steinmeyer, D. H. Sutter, L. Gallmann, N. Matuschek, U. Keller, *Science* **286**, 1507–1512 (1999).
- P. M. Paul et al., *Science* **292**, 1689–1692 (2001).
- M. Hentschel et al., *Nature* **414**, 509–513 (2001).
- H. Telle et al., *Appl. Phys. B* **69**, 327–332 (1999).
- E. Goulielmakis et al., *Nature* **466**, 739–743 (2010).
- H. Wang et al., *Phys. Rev. Lett.* **105**, 143002 (2010).
- M. Holler, F. Schapper, L. Gallmann, U. Keller, *Phys. Rev. Lett.* **106**, 123601 (2011).
- M. Schultze et al., *Nature* **493**, 75–78 (2013).
- M. Schultze et al., *Science* **346**, 1348–1352 (2014).
- H. Mashiko, K. Oguri, T. Yamaguchi, A. Suda, H. Gotoh, *Nat. Phys.* **10**, 1038/nphys3711 (2016).
- F. Krausz, M. I. Stockman, *Nat. Photonics* **8**, 205–213 (2014).
- H. J. Caulfield, S. Dolev, *Nat. Photonics* **4**, 261–263 (2010).
- A. H. Chin, J. M. Bakker, J. Kono, *Phys. Rev. Lett.* **85**, 3293–3296 (2000).
- Y. Mizumoto, Y. Kayanuma, A. Srivastava, J. Kono, A. H. Chin, *Phys. Rev. B* **74**, 045216 (2006).
- A. P. Jauho, K. Johnsen, *Phys. Rev. Lett.* **76**, 4576–4579 (1996).
- G. H. Wannier, *Elements of Solid State Theory* (Cambridge Univ. Press, 1960).
- G. Vampa et al., *Nature* **522**, 462–464 (2015).
- T. T. Luu et al., *Nature* **521**, 498–502 (2015).
- P. Y. Yu, M. Cardona, *Fundamentals of Semiconductors* (Springer, ed. 4, 2010).
- F. Novelli, D. Fausti, F. Giusti, F. Parmigiani, M. Hoffmann, *Sci. Rep.* **3**, 1227 (2013).
- A. Srivastava, R. Srivastava, J. Wang, J. Kono, *Phys. Rev. Lett.* **93**, 157401 (2004).
- K. B. Nordstrom et al., *Phys. Rev. Lett.* **81**, 457–460 (1998).
- R. Locher et al., *Rev. Sci. Instrum.* **85**, 013113 (2014).
- See supplementary materials on Science Online.
- L. V. Keldysh, *Sov. Phys. J. Exp. Theor. Phys.* **20**, 1307 (1965).
- S. A. Sato, K. Yabana, Y. Shinohara, T. Otobe, G. F. Bertsch, *Phys. Rev. B* **89**, 064304 (2014).
- K. Yabana, T. Sugiyama, Y. Shinohara, T. Otobe, G. F. Bertsch, *Phys. Rev. B* **85**, 045134 (2012).
- W. V. Houston, *Phys. Rev.* **57**, 184–186 (1940).
- T. Otobe, Y. Shinohara, S. A. Sato, K. Yabana, *Phys. Rev. B* **93**, 045124 (2016).

#### ACKNOWLEDGMENTS

Supported by the National Center of Competence in Research Molecular Ultrafast Science and Technology (NCCR MUST) funded by the Swiss National Science Foundation, and by JSPS KAKENHI grants 15H03674 and 26-1511. This research used computational resources of the K computer provided by RIKEN AICS through the HPCI System Research project (Project ID hp150101), and was supported in part by MEXT as a priority issue theme 7 to be tackled by using Post K Computer.

#### SUPPLEMENTARY MATERIALS

www.sciencemag.org/content/353/6302/916/suppl/DC1  
Materials and Methods  
Figs. S1 to S13  
References (33–45)

12 May 2016; accepted 27 July 2016  
10.1126/science.aag1268

## GEOPHYSICS

# Teleseismic *S* wave microseisms

Kiwamu Nishida<sup>1\*</sup> and Ryota Takagi<sup>2</sup>

Although observations of microseisms excited by ocean swells were firmly established in the 1940s, the source locations remain difficult to track. Delineation of the source locations and energy partition of the seismic wave components are key to understanding the excitation mechanisms. Using a seismic array in Japan, we observed both *P* and *S* wave microseisms excited by a severe distant storm in the Atlantic Ocean. Although nonlinear forcing of an ocean swell with a one-dimensional Earth model can explain *P* waves and vertically polarized *S* waves (*SV* waves), it cannot explain horizontally polarized *S* waves (*SH* waves). The precise source locations may provide a new catalog for exploring Earth's interior.

**M**icroseisms are ambient seismic wavefields (*I*) that occur in the 0.05- to 0.5-Hz frequency range. Although they had been recognized as ambient noise for seismic observation, a new technique known as seismic interferometry turned them into signals for exploring Earth's interior (2). They can be categorized into two groups according to the typical frequencies. The first group is classified as primary microseisms ranging from 0.05 to 0.1 Hz, which corresponds to the typical frequency of ocean swells. The second is classified as secondary microseisms ranging from 0.1 to 0.5 Hz, which doubles the frequency of an ocean swell, indicating that the secondary microseisms are generated through nonlinear wave-wave interactions (3, 4). They excite surface waves dominantly.

*P* wave microseisms from distant storms have been studied (5, 6) by means of array analysis of dense seismic data. Source locations of the *P* wave provided a better spatial localization of the excitation source than that of surface waves. The estimated source distribution was consistent with a theoretical estimation that uses wave action models. Most studies, however, have focused only on *P* waves recorded as vertical components because of the larger amplitudes. Although *S* wave amplitudes are estimated to be one order of magnitude smaller than *P* wave amplitudes (7, 8), the precise locations of *P* and *S* waves can help in understanding the excitation mechanism.

The energy partition between Love and Rayleigh waves is another key parameter for understanding the force system of excitation sources. The force system can be characterized by the surface pressure source and/or shear traction on the seafloor (9). The observed dominance of Love waves in primary microseisms suggests that they are generated by pressure loadings of an ocean swell acting on a sloping coast (10). However, the scattering of surface waves during propagation distorts the energy ratio at the source area. Because the teleseismic body waves are less scattered, the energy partition between *P* and *S* waves is more appropriate for understanding the source mechanism. However, the smaller body-wave amplitudes at a distance

tend to be masked by the surface waves owing to local ocean swell activities (8, 11, 12).

For the detection of both *P* and *S* wave microseisms, we conducted an array analysis using 202 Hi-net stations operated by the National Research Institute for Earth Science and Disaster Prevention (NIED) in Chugoku district, where the crustal heterogeneity is weak in Japan (Fig. 1A). NIED deployed three-component velocity meters with a natural frequency of 1 Hz at the bottom of a borehole of each station. We deconvolved the instrumental response using the inverse filtering technique (13) after the reduction of common logger noise (14) so as to use low-frequency components below 1 Hz. We analyzed data of a rapidly deepening cyclonic low-pressure area known as a “weather bomb” (15), with a central pressure of ~940 hPa that developed in the Atlantic between Iceland and Greenland on 9–11 December 2014 (16). The system was a typical explosive cyclogenesis, with a reduction of 24 hPa in 24 hours on 9 December. We divided the records into 1024-s segments. After the exclusion of noisy data, we calculated two-dimensional (2D) frequency-slowness spectra (9) in the 0.1- to 0.2-Hz frequency window (Fig. 1B), assuming that signals at a station can be represented by a superposition of plane waves. The spectrum at a certain slowness vector represents the sum of all the records, with the predicted time delays. The spectra have local maxima in the slowness domain, where signals recorded at all the stations are in phase.

The spectra of the vertical and radial components displayed a clear teleseismic *P* wave. The slowness of ~0.05 s/km and the back azimuth of ~5° were consistent with that of a *P* wave traveled from the Atlantic Ocean. The dominant *P* wave can be explained by the nonlinear forcing by ocean swell (7) according to Longuet-Higgins's theory (3), which can be equivalently represented by a vertical single force on the sea surface.

The spectrum of the radial component showed not only a *P* wave but also a rarely seen *SV* wave (8), with mean square (MS) amplitude of ~8% of the *P* wave amplitude. The observed slowness of the *SV* wave suggests that the source could be located in the same area of the *P* wave microseisms in the Atlantic Ocean. The simplest mechanism of the observed *S* wave excitation is the *P*-to-*SV* conversion on the sea bottom during multiple reflections within the ocean (7). Although the theoretical MS amplitude (7) of an *SV* wave is two orders smaller than

<sup>1</sup>Earthquake Research Institute, University of Tokyo, 1-1-1 Yayoi 1, Bunkyo-ku, Tokyo 113-0032, Japan. <sup>2</sup>Research Center for Prediction of Earthquakes and Volcanic Eruptions, Graduate School of Science, Tohoku University, 6-6 Aza-Aoba, Aramaki, Aoba-ku, Sendai 980-8578, Japan.

\*Corresponding author. E-mail: knishida@eri.u-tokyo.ac.jp



## Attosecond dynamical Franz-Keldysh effect in polycrystalline diamond

M. Lucchini, S. A. Sato, A. Ludwig, J. Herrmann, M. Volkov, L. Kasmi, Y. Shinohara, K. Yabana, L. Gallmann and U. Keller  
(August 25, 2016)  
*Science* **353** (6302), 916-919. [doi: 10.1126/science.aag1268]

Editor's Summary

### Shining a fast light on diamonds

Conceptually, the electronic structure of matter is a fixed scaffold of energy levels, which electrons climb with the help of light absorption. In reality, the light's electromagnetic field distorts the scaffold, a phenomenon that becomes increasingly evident with rising field intensity. Lucchini *et al.* studied a manifestation of this phenomenon, termed the dynamical Franz Keldysh effect, in diamond substrates exposed to sudden, moderately intense infrared fields. Using attosecond probe pulses and accompanying theoretical simulations, they resolved and accounted for the extremely rapid ensuing electron dynamics.

*Science*, this issue p. 916

---

This copy is for your personal, non-commercial use only.

---

**Article Tools** Visit the online version of this article to access the personalization and article tools:  
<http://science.sciencemag.org/content/353/6302/916>

**Permissions** Obtain information about reproducing this article:  
<http://www.sciencemag.org/about/permissions.dtl>

*Science* (print ISSN 0036-8075; online ISSN 1095-9203) is published weekly, except the last week in December, by the American Association for the Advancement of Science, 1200 New York Avenue NW, Washington, DC 20005. Copyright 2016 by the American Association for the Advancement of Science; all rights reserved. The title *Science* is a registered trademark of AAAS.